



# Maximizing the utilization of single-atom sites on carbon-based catalysts for efficient CO<sub>2</sub> electroreduction with ultrahigh turnover frequency

Shuyu Liang<sup>a,b</sup>, Tianyu Zhang<sup>a,b,\*</sup>, Yue Zheng<sup>a,b</sup>, Tianshan Xue<sup>c</sup>, Zheng Wang<sup>d</sup>,  
Qiang Wang<sup>a,b,\*</sup>, Hong He<sup>d</sup>

<sup>a</sup> Beijing Key Lab for Source Control Technology of Water Pollution, College of Environmental Science and Engineering, Beijing Forestry University, Beijing 100083, PR China

<sup>b</sup> Engineering Research Center for Water Pollution Source Control & Eco-remediation, College of Environmental Science and Engineering, Beijing Forestry University, Beijing 100083, PR China

<sup>c</sup> Institute of Atmospheric Environment, Chinese Academy of Environmental Sciences, Beijing 100012, PR China

<sup>d</sup> Laboratory of Atmospheric Environment and Pollution Control, Research Center for EcoEnvironmental Sciences, Chinese Academy of Sciences, Beijing 100085, PR China

## ARTICLE INFO

### Keywords:

CO<sub>2</sub> electroreduction  
Single-atom catalysts  
Active sites utilization  
Ultrahigh turnover frequency

## ABSTRACT

Increasing the amount of accessible active sites to reactants is an effective way to enhance electrocatalytic activity. Although single-atom catalysts are claimed to be capable of achieving 100% atomic utilization, there may be abundant single-atom sites buried and inaccessible to reactants in practice. Herein, two Ni, N-doped carbon catalysts with Ni-N<sub>x</sub> atomic sites are comparatively studied for CO<sub>2</sub> electroreduction. In contrast to the Ni-N<sub>x</sub>/Carbon nanosheets with Ni loading of 2.42 wt%, the Ni-N<sub>x</sub>/Carbon black with lower Ni loading of 0.16 wt% excitingly exhibits higher activity for CO production. The atomically dispersed Ni-N<sub>x</sub> sites over carbon black surface benefit the exposure and utilization of single-atom sites, leading to a significant increase of TOF from 2140 to 100,347 h<sup>-1</sup> at -0.8 V. Particularly, an extraordinarily high current density up to 300 mA cm<sup>-2</sup> with CO selectivity of ~100 % are achieved for Ni-N<sub>x</sub>/CB in the flow cell. This work demonstrates the significance of increasing single-atom site utilization.

## 1. Introduction

CO<sub>2</sub> electroreduction (CO<sub>2</sub>RR) provides a promising way to alleviate CO<sub>2</sub> emission and produce value-added fuels and chemicals at the same time [1–4]. Among various CO<sub>2</sub>RR pathways, CO<sub>2</sub> electroreduction to CO shows good application prospects because of its high achievable selectivity approaching 100 % [5–7]. Moreover, the gaseous CO is easy to be separated from the liquid electrolyte and can serve as a component of syngas for Fischer-Tropsch synthesis [8,9].

Over the past few years, some efficient catalysts for CO production were studied, including noble metals (e.g., Au, Ag), metal-free carbon-based materials, and transition metal carbon-based catalysts [10–14]. Considering the trade-off between catalyst cost and its electrocatalytic performance, the earth-abundant transition metal N-doped carbon catalysts (M-N-C) containing atomically dispersed M-N<sub>x</sub> active sites have been widely applied for electrolysis [15,16] and have become the most

promising candidate for large-scale CO production, which could achieve high atomic efficiency and reach high CO selectivity towards CO<sub>2</sub>RR [17–22]. Especially, among different transition metals, Ni-N-C catalysts with atomically dispersed Ni-N<sub>x</sub> sites have suggested superb CO selectivity over 90 % in a wide potential range because of the most positive limiting potential difference between CO<sub>2</sub>RR and HER [23–26]. In general, there are three ways to improve the CO<sub>2</sub>RR performance of M-N-C catalysts: (1) Enhancing the intrinsic activity through adjusting the surrounding coordination environment of the central metal atoms; (2) Increasing the amount of accessible active single-atoms; (3) Modulating the morphological structure of carbon matrix to improve the mass transport.

In recent years, most studies have focused on regulating the coordination environment that Ni-N-C catalysts with various dominant moieties including Ni-N<sub>3</sub>, Ni-N<sub>4</sub>, Ni-N<sub>x</sub>C<sub>4-x</sub> (x = 1–3), and coordinatively unsaturated Ni-N sites have been extensively studied

\* Corresponding authors at: Beijing Key Lab for Source Control Technology of Water Pollution, College of Environmental Science and Engineering, Beijing Forestry University, Beijing 100083, PR China

E-mail addresses: [tzhang@bjfu.edu.cn](mailto:tzhang@bjfu.edu.cn) (T. Zhang), [qiangwang@bjfu.edu.cn](mailto:qiangwang@bjfu.edu.cn) (Q. Wang).

<https://doi.org/10.1016/j.apcatb.2023.122801>

Received 19 September 2022; Received in revised form 5 April 2023; Accepted 21 April 2023

Available online 23 April 2023

0926-3373/© 2023 Elsevier B.V. All rights reserved.

[27–31]. We have summarized the CO<sub>2</sub>RR performance of these reported Ni-N-C catalysts with distinct Ni-N<sub>x</sub> sites in a previous review [32], which all suggest high CO FE over 90 %, but the CO partial current density is not always proportional to the Ni loading in different single-Ni-atom catalysts. For example, a single-Ni-atom catalyst on commercial carbon black with a low Ni loading of 0.27 wt% achieved a high current of more than 8 A in a  $10 \times 10 \text{ cm}^{-2}$  flow cell, superior to many other single-Ni-atom catalysts. [33] In contrast, Ni single atoms on graphene nanosheets with a Ni loading of  $\sim 2.07 \text{ wt\%}$  reported by the same group suggested a lower CO partial current density under the same operation condition (around  $12 \text{ mA cm}^{-2}$  vs  $20 \text{ mA cm}^{-2}$  under  $-0.9 \text{ V}$  vs RHE in H-type cell). [34] Although the current density can be affected by many factors other than catalyst activity, it is still worth noting. The development of high-loading or ultrahigh-loading single-atom catalysts is arising as a hopeful way to enhance the activity in the field of electrocatalysis recently [24,35,36]. Besides, some of the ultrahigh-loading single-atom catalysts have exhibited excellent catalysis performance, but their single-atom site utilization is likely to be less than 100 % [35, 37–39]. For example, Malko et al. found that the utilization rate of FeN<sub>x</sub> sites in Fe/N/C SACs was only 4.5 % by nitrite adsorption and followed reductive stripping method, which suggested that the single-atom catalyst has huge activity potential by increasing the utilization of the active sites [40]. This reminds us to pay attention to the utilization of single-atom sites while focusing on improving single-atom loading.

However, the nitrite adsorption method for the quantification of the accessible active sites is unfortunately limited to Fe-N-C catalysts, while another versatile in situ method proposed by Choi et al. needs to employ a highly toxic cyanide anion probe [41]. Therefore, it is difficult to precisely quantify the utilization rate of single-atom sites during the reaction. Considering that the reaction is carried out over the surface of the catalyst, it is highly significant to increase the effective active sites that can be accessible to the reactants. Facile and scalable synthesis of the single-atom catalyst with more active sites accessible to reactants should become a priority for industrial CO<sub>2</sub> electrolysis.

Herein, we visually compared the performance of two single-Ni-atom catalysts with different Ni contents to indicate the significance of the single-atom accessibility to the reactant. We used biomolecule guanine

as the sole carbon and nitrogen source to fabricate single Ni atoms onto carbon nanosheets (Ni-N<sub>x</sub>/CNS). By further introducing commercial carbon black (Cabot Vulcan XC-72) as carbon support to the above synthesis, gram-level carbon black-supported Ni single-atom catalyst (Ni-N<sub>x</sub>/CB) with three-dimensional morphology can be achieved via a facile and scalable approach (Fig. 1). The characterization results clearly demonstrated that Ni was atomically dispersed throughout the guanine derived carbon or carbon black support for both two catalysts. Interestingly, Ni-N<sub>x</sub>/CB with a lower Ni content of 0.16 wt% reversely reached superior performance for CO production during a wider potential range to Ni-N<sub>x</sub>/CNS with a higher Ni content of 2.42 wt%. The introduction of carbon black facilitates the formation of more surface dispersed single Ni-N sites that are accessible to reactants and enhanced the mass transport, by which the TOF calculation based on Ni mass activity for Ni-N<sub>x</sub>/CB reached an ultrahigh value up to  $100347 \text{ h}^{-1}$  at  $-0.8 \text{ V}$  vs RHE.

## 2. Experimental section

### 2.1. Synthesis of catalysts

For the synthesis of Ni-N<sub>x</sub>/CNS, 1 g guanine and 0.5 mL Ni(NO<sub>3</sub>)<sub>2</sub>·6 H<sub>2</sub>O solution ( $0.1 \text{ mmol mL}^{-1}$ ) were added into 60 mL deionized (D.I.) water and stirred for 4 h under room temperature. The obtained solution was then evaporated in a rotary evaporator under  $80^\circ\text{C}$  to get a light-yellow powder. Subsequently, the prepared powder was pyrolyzed at  $900^\circ\text{C}$  ( $5^\circ\text{C min}^{-1}$ ) for 1 h under continuous N<sub>2</sub> flow. The Ni-N<sub>x</sub>/CNS-0.12 wt%, and Ni-N<sub>x</sub>/CNS-0.22 wt% samples were also prepared by a similar procedure, except that the volume of Ni(NO<sub>3</sub>)<sub>2</sub>·6 H<sub>2</sub>O solution ( $0.1 \text{ mmol mL}^{-1}$ ) added was 0.02 mL and 0.05 mL, respectively. For the synthesis of Ni-N<sub>x</sub>/CB, 1 g guanine and 0.5 mL Ni(NO<sub>3</sub>)<sub>2</sub>·6 H<sub>2</sub>O solution ( $0.1 \text{ mmol mL}^{-1}$ ) were added into 60 mL D.I. water and stirred for 10 min, then 2 g carbon black (Cabot Vulcan XC-72) was added into the solution and stirred for 4 h. The following steps were the same as the synthesis of Ni-N<sub>x</sub>/CNS.

Ni-N<sub>x</sub>/CB<sub>x</sub> with different weight ratios of guanine to carbon black (1:0.1, 1:0.6, 1:2) were prepared at  $900^\circ\text{C}$  in N<sub>2</sub> flow. Besides, another

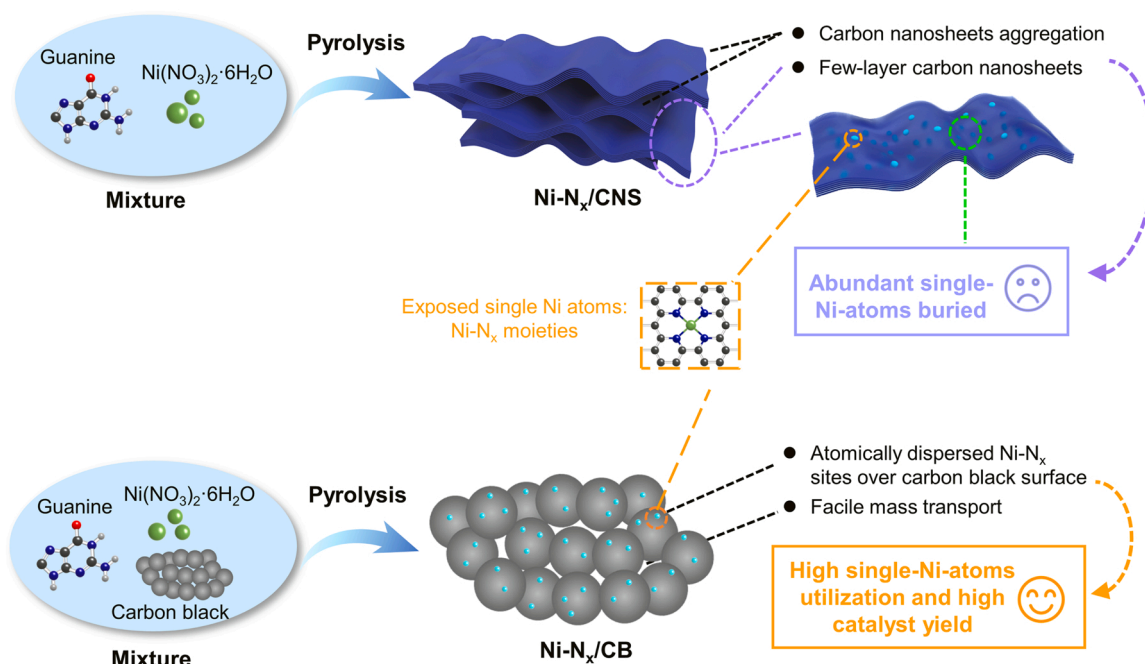


**Fig. 1.** Schematic illustration of the synthesis process of Ni-N<sub>x</sub>/CNS and Ni-N<sub>x</sub>/CB with dominant Ni-N<sub>x</sub> moieties. For Ni-N<sub>x</sub>/CNS, abundant single-Ni-atoms were buried in the few-layer carbon nanosheets. For Ni-N<sub>x</sub>/CB, the atomically dispersed Ni-N<sub>x</sub> sites over the carbon black particles surface led to high single-Ni-atoms utilization.

two commercial carbon blacks (including Ketjenblack ECP600JD, Cabot BP-2000) were also used as carbon precursor to prepare single-Ni-atom catalysts with a weight ratio of guanine to carbon black = 1:0.5, 1:1, 1:2, donated as Ni-N<sub>x</sub>/CB<sub>1:0.5</sub>(ECP-600JD), Ni-N<sub>x</sub>/CB<sub>1:1</sub>(ECP-600JD), Ni-N<sub>x</sub>/CB<sub>1:1</sub>(BP-2000) and Ni-N<sub>x</sub>/CB<sub>1:2</sub>(BP-2000), respectively. The Ni-N<sub>x</sub>/CB-0.07 wt%, and Ni-N<sub>x</sub>/CB-0.77 wt% samples were also prepared by a similar procedure, except that the volume of Ni(NO<sub>3</sub>)<sub>2</sub>·6 H<sub>2</sub>O solution (0.1 mmol mL<sup>-1</sup>) added was 0.1 mL and 2.5 mL, respectively. Besides, the preparation of Ni-N<sub>x</sub>/CB was scaled-up to 6 times, with 6 g guanine, 12 g carbon black and 3.0 mL Ni(NO<sub>3</sub>)<sub>2</sub>·6 H<sub>2</sub>O solution (0.1 mmol mL<sup>-1</sup>) mixed in D.I. water, and evaporated in a beaker instead of in a rotary evaporator. The following preparation steps are the same, and 12.69 g of Ni-N<sub>x</sub>/CB was obtained finally.

For the synthesis of NC, 1 g guanine was pyrolyzed at 900 °C for 1 h in continuous N<sub>2</sub> flow. For the synthesis of NCB, 2 g carbon black and 1 g guanine were directly pyrolyzed and the other procedures were the same.

## 2.2. Catalyst characterization

The morphology of samples was characterized by field emission scanning electron microscopy (FESEM, SU8010), transmission electron microscopy (TEM, JEM-2100 F), and the high-angle annular dark-field transmission electron microscope (HAADF-STEM, JEM-ARM200F). The X-ray powder diffraction (XRD, Shimadzu-7000) was used to examine the crystal structures. The surface composition of catalysts was analysed by X-ray photoelectron spectroscopy (XPS, Thermo Scientific ESCALAB 250Xi). The Ni content in catalysts was detected by inductively coupled plasma (ICP) and the C and N content was detected by an elemental analyzer (Vario MACRO Cube). The Brunauer-Emmett-Teller (BET) specific surface area of catalysts were examined through N<sub>2</sub> adsorption/desorption test on a physisorption analyzer (SSA-7000, Builder). The X-ray absorption spectroscopy (XAS) experiments were conducted at the BSRF 1W1B beamline in Beijing. The Ni K-edge data collections were taken in fluorescence mode. Data analysis and EXAFS fitting were performed by using Athena and Artemis programs [42] and FEFF6 program [43]. TGA analysis during the pyrolysis of precursors for Ni-N<sub>x</sub>/CNS and Ni-N<sub>x</sub>/CB preparation was performed by using a TGA analyzer (Q50 TA Instrument) in high purity N<sub>2</sub> gas (20 mL min<sup>-1</sup>) from 25 °C to 900 °C (5 °C min<sup>-1</sup>). In situ attenuated total reflection-infrared spectroscopy (ATR-IR) was performed on a Nicolet iS50 FT-IR spectrometer equipped with an MCT detector. The catalyst was loaded on the Au/Si substrate. During the test, the linear sweep voltammetry (LSV) tests were performed in CO<sub>2</sub>-saturated 0.5 M KHCO<sub>3</sub> electrolyte during a potential range of -0.4 to -1.1 V (3 mV s<sup>-1</sup>).

## 2.3. Electrochemical measurements

The electrochemical measurements were conducted in a commercial H-type cell containing electrolyte of 0.5 M KHCO<sub>3</sub>. A Pt mesh and an Ag/AgCl electrode were used as the counter electrode and the reference electrode, respectively. 10 mg of catalysts were mixed with 1 mL of ethanol and 20 μL of Nafion solution (5 %), and sonicated for 40 min to generate a uniform ink. Subsequently, the ink was dropped onto a carbon paper to obtain a loading amount of ~1 mg cm<sup>-2</sup> and dried in air to obtain the working electrode for constant electrolysis. LSV tests were conducted in N<sub>2</sub>- or CO<sub>2</sub>-saturated 0.5 M KHCO<sub>3</sub> electrolyte from 0 to -1.0 V vs. RHE (20 mV s<sup>-1</sup>). The electrochemically active surface area (ECSA) was calculated by performing cyclic voltammetry at a series of scanning rates (10 ~ 100 mV s<sup>-1</sup>). The Tafel slope was detected from the constant electrolysis from overpotential (η) of 0.35 ~ 0.5 V, which was calculated according to the equation: η = log(j<sub>CO</sub>/j<sub>total</sub>), where η represents the overpotential, b represents the Tafel slope, j<sub>CO</sub> and j<sub>total</sub> are CO partial current density and total current density, respectively. The electrochemical impedance spectroscopy (EIS) tests were performed by applying at -0.6 V vs. RHE with 5 mV amplitude in the frequency

range of 100 kHz ~ 100 mHz. TOF for CO production was calculated from the Eq. (2.1), where j<sub>CO</sub> is the CO partial current density, n is the number of electrons transferred for CO formation, F is the Faraday's constant (96,485 C mol<sup>-1</sup>), m<sub>cat</sub> is the catalyst loading on the electrode (0.01–3 mg cm<sup>-2</sup>), w is the Ni loading of the catalyst, M<sub>Ni</sub> is the atomic mass of Ni (58 g mol<sup>-1</sup>).

$$\text{TOF}(h^{-1}) = \frac{j_{\text{CO}}/nF}{m_{\text{cat}} \times w/M_{\text{Ni}}} \times 3600 \quad (2.1)$$

## 2.4. CO<sub>2</sub> products analysis

During the CO<sub>2</sub> electroreduction reaction, high-purity CO<sub>2</sub> gas continuously flowed into the electrolyte with a flow rate of around 20 mL min<sup>-1</sup>. The gas products were detected by the online gas chromatograph (Shimadzu GC-2014 C) every 7.5 min. The Faradaic efficiency of the gas products was calculated through Eq. (2.2), where Q<sub>i</sub> is the charge used for certain product production (C), Q<sub>total</sub> is the total charge passed during the reaction (C), N<sub>i</sub> is the number of moles for a certain product tested by GC (mol), n is the number of electrons transferred for CO production, F is the Faraday's constant.

$$\text{FE} = \frac{Q_i}{Q_{\text{total}}} = \frac{N_i \times n \times F}{Q_{\text{total}}} \quad (2.2)$$

N<sub>i</sub> can be calculated from the following equation (Eq. (2.3)), where P<sub>0</sub> represents atmosphere pressure (1.013 × 10<sup>5</sup> Pa), T represents the reaction temperature (298 K), R represents the ideal gas constant (8.314 J mol<sup>-1</sup> K<sup>-1</sup>), v represents the outlet flow rate (mL min<sup>-1</sup>), t is the time for gas to fill the GC sampling loop, c is the product concentration detected by GC.

$$N_i = \frac{P_0 \times v \times t}{R \times T} \times c \quad (2.3)$$

## 2.5. Flow cell measurements

The CO<sub>2</sub>RR performance were further carried out in a self-made microflow cell, which is composed of gas, catholyte and anolyte chambers (Fig. 5a). The catalyst ink was dropped on a Toray YLS30T gas diffusion layer (GDL) to achieve a catalyst loading of ~1 mg cm<sup>-2</sup>. The Ag/AgCl, and Pt foil were used as reference electrode and anode, respectively. The catholyte chamber and anolyte chamber were separated by an anion exchange membrane (Fumasep FAB-PK-130). During the measurements, CO<sub>2</sub> was transferred into the gas chamber behind the gas diffusion electrode at a flow rate of around 20 mL min<sup>-1</sup>, and a bubble flowmeter was used to measure the flow rate at the outlet of the electrolytic cell. The catholyte and anolyte (both 1 M KOH) were continuously circulated by peristaltic pumps with a flow rate of 10 mL min<sup>-1</sup>. A current amplifier (CHI680C) was used to connect with the electrochemical workstation (CHI660e) to broaden the current range. For each potential test, the potential was manually corrected using the following formula: E = E/applied - iR<sub>s</sub> (E/applied is the applied potential, i is the measured current, R<sub>s</sub> was obtained through EIS measurements).

## 2.6. Zn-CO<sub>2</sub> battery

The charge-discharge tests of the Zn-CO<sub>2</sub> battery with Ni-N<sub>x</sub>/CB as cathode were fulfilled in a two-compartment cell separated by a bipolar membrane. A Zn plate was used as the anode after polishing. The cathodic electrolyte was CO<sub>2</sub>-saturated 0.8 M KHCO<sub>3</sub>, and the anodic electrolyte was 0.8 M KOH + 0.02 M Zn(Ac)<sub>2</sub>. During the charge-discharge tests, CO<sub>2</sub> continuously flowed into the catholyte at a flow rate of 10 mL min<sup>-1</sup>.



### 3. Results and discussion

#### 3.1. Samples synthesis and characterization

To study the importance of the single-atom accessibility to the reactant for electrocatalytic reaction, two-dimensional (2D) single-Ni-atom N-doped carbon catalyst (Ni-N<sub>x</sub>/CNS) and three-dimensional (3D) Ni single-atom catalyst (Ni-N<sub>x</sub>/CB) were directly prepared via one-step pyrolysis approach. The Ni-N<sub>x</sub>/CNS was obtained from a mixture of guanine and Ni(NO<sub>3</sub>)<sub>2</sub>·6 H<sub>2</sub>O at 900 °C in N<sub>2</sub> flow, without subsequent acid treatment. While the preparation of Ni-N<sub>x</sub>/CB followed the same procedure except for the addition of carbon black (Fig. 1). For comparison, Ni-free NCNS (pyrolyzed by guanine) and NCB (pyrolyzed by guanine and carbon black) catalysts were also fabricated using the same method. The detailed synthetic steps are shown in the

experimental section. The pyrolysis processes of Ni-N<sub>x</sub>/CNS and Ni-N<sub>x</sub>/CB were examined by thermogravimetric analysis in N<sub>2</sub> flow (Fig. S1). Due to the addition of carbon black precursor, the yield of the Ni-N<sub>x</sub>/CB catalyst was significantly increased by 12 times of Ni-N<sub>x</sub>/CN.

Ni-N<sub>x</sub>/CNS displayed smooth curly 2D nanosheets morphology similar to the guanine-derived NCNS, with a thickness of 1.4 nm determined by AFM characterization (Fig. 2a and Fig. S2). While after introducing carbon black (with a BET-specific surface area of 419 m<sup>2</sup> g<sup>-1</sup>) as support, Ni-N<sub>x</sub>/CB, NCB and CB showed almost identical spherical particle morphology with a size of 20–50 nm (Fig. 2b and Fig. S3). TEM and HAADF-STEM images for the Ni-N<sub>x</sub>/CNS and Ni-N<sub>x</sub>/CB confirmed no Ni nanoparticles were observed on the carbon black support (Fig. 2a-d). The HR-TEM image suggested distinct lattice fringes with a spacing of 0.34 nm, which can be attributed to the (002) plane of graphitic carbon (Fig. S4). The Raman spectrum (Fig. S5) also indicated

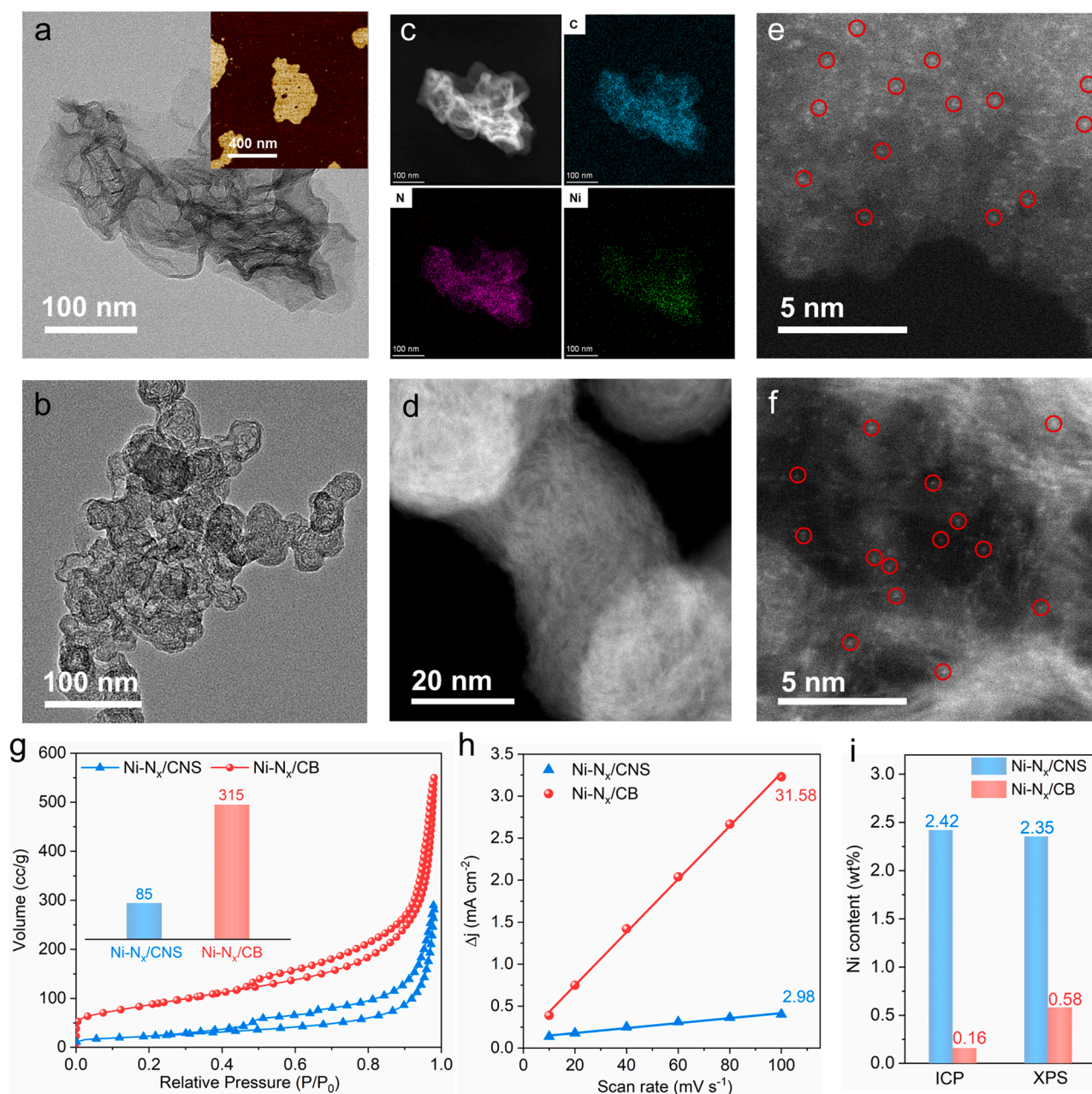


**Fig. 2.** Morphological characterization of the samples. (a) HRTEM and AFM images (Inset) for Ni-N<sub>x</sub>/CNS. (b) HRTEM image for Ni-N<sub>x</sub>/CB. (c) STEM and corresponding EDX elemental mapping for Ni-N<sub>x</sub>/CNS. (d) HAADF-STEM image for Ni-N<sub>x</sub>/CB. (e-f) HAADF-STEM images for Ni-N<sub>x</sub>/CNS and Ni-N<sub>x</sub>/CB, respectively. (g) N<sub>2</sub> adsorption-desorption isotherms, (h) Double-layer capacitance, (i) Ni content determined by XPS and ICP-MS for Ni-N<sub>x</sub>/CNS and Ni-N<sub>x</sub>/CB.



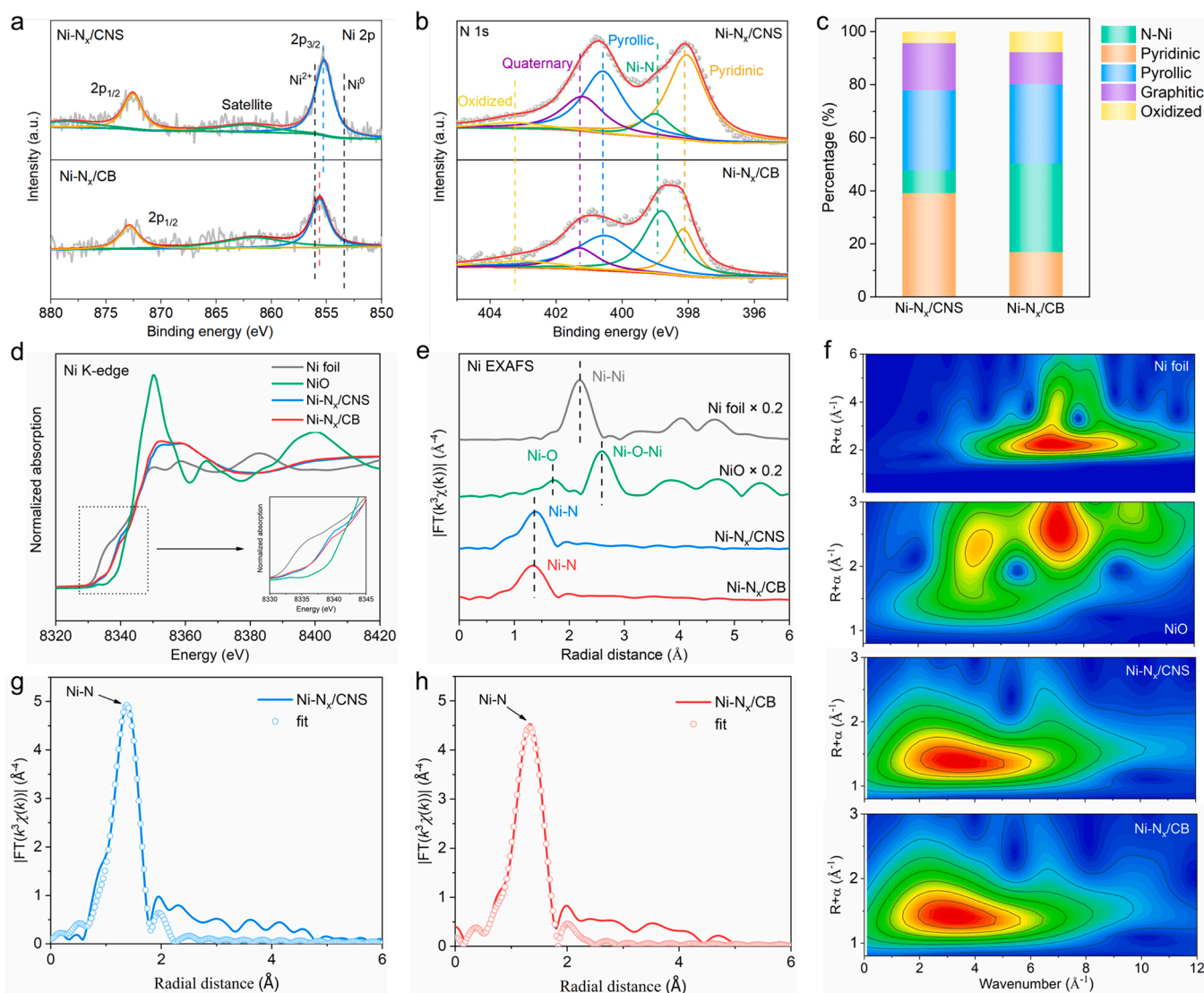
that the graphitic content of the carbon support increased after pyrolysis during Ni-N<sub>x</sub>/CB preparation since the I<sub>D</sub>/I<sub>G</sub> ratio for Ni-N<sub>x</sub>/CB of 1.05 was lower than that for pristine carbon black (I<sub>D</sub>/I<sub>G</sub> = 1.31). Elemental mappings (Fig. 2c) suggested uniform distribution of C, N and Ni elements over the carbon support for Ni-N<sub>x</sub>/CNS catalysts, while for Ni-N<sub>x</sub>/CB catalyst, it is hard to obtain the accurate distribution of Ni because of its low content. The aberration-corrected HAADF-STEM image proved the existence of atomically dispersed Ni species as bright spots for both Ni-N<sub>x</sub>/CNS and Ni-N<sub>x</sub>/CB (Fig. 2e and f).

Fig. 2g indicates Ni-N<sub>x</sub>/CB with particle morphology had a higher BET-specific surface area of 315 m<sup>2</sup> g<sup>-1</sup> as well as a higher total porous volume of 0.85 cm<sup>3</sup> g<sup>-1</sup> than Ni-N<sub>x</sub>/CNS with nanosheets morphology (85 m<sup>2</sup> g<sup>-1</sup> and 0.46 cm<sup>3</sup> g<sup>-1</sup>). Both Ni-N<sub>x</sub>/CNS and Ni-N<sub>x</sub>/CB are rich in mesopores (Fig. S6). Correspondingly, the ECSA was also obtained on the basis of the double-layer capacitance (C<sub>dl</sub>) of the electrode by performing a series of CV measurements (Fig. 2h). The C<sub>dl</sub> of Ni-N<sub>x</sub>/CB and Ni-N<sub>x</sub>/CNS catalysts was 31.58 mF cm<sup>-2</sup> and 2.98 mF cm<sup>-2</sup>, respectively. The ECSA of Ni-N<sub>x</sub>/CB was then calculated to be 1503.8 cm<sup>2</sup>, significantly higher than that of Ni-N<sub>x</sub>/CNS (141.9 cm<sup>2</sup>). After introducing carbon black, the BET-specific surface area and the surface roughness of Ni-N<sub>x</sub>/CB were largely improved compared to Ni-N<sub>x</sub>/CNS,

which is beneficial to expose more active sites and enhancing mass transfer.

The content of Ni, N, and C in Ni-N<sub>x</sub>/CNS determined by ICP-MS and elemental analyser was 2.42 wt%, 16.02 wt%, and 69.90 wt%, respectively. While after introducing carbon black support, the Ni and N content in Ni-N<sub>x</sub>/CB was significantly decreased to 0.16 wt% and 0.59 wt% with the C content increased to 90.08 wt% (Fig. 2i). For 2D Ni-N<sub>x</sub>/CNS, the mass fraction of Ni measured by ICP and XPS are very close (2.42 wt% and 2.35 wt%, respectively), while for 3D Ni-N<sub>x</sub>/CB the mass fraction of Ni determined by XPS (0.58 wt%) is higher than that by ICP (0.16 wt%), indicating Ni single atoms are more concentrated on the surface of carbon black particles. XRD patterns in Fig. S7 showed that for all the prepared samples, two diffraction peaks centered at 24° (or 26.2°) and 43.5° appeared, which can be assigned to the (002) and (100) planes of the graphite [44]. Importantly, no metallic peak was observed for all samples, indicating low Ni content in Ni-N<sub>x</sub>/CNS and Ni-N<sub>x</sub>/CB catalysts.

The elemental composition and chemical status of catalysts were further analyzed via XPS. The wide-survey spectrum confirmed the presence of Ni, N, C and O elements in Ni-N<sub>x</sub>/CNS and Ni-N<sub>x</sub>/CB catalysts (Fig. S8). Ni-N<sub>x</sub>/CB had higher C content (97.65 at%) and lower N



**Fig. 3.** Structural characterization of the samples. (a) XPS spectrum of Ni 2p, (b) XPS spectrum of N 1 s, (c) N composition derived from N 1 s XPS for Ni-N<sub>x</sub>/CNS and Ni-N<sub>x</sub>/CB. (d) Ni K-edge XANES spectra, (e) Fourier transformation of EXAFS spectra for Ni foil, NiO, Ni-N<sub>x</sub>/CNS and Ni-N<sub>x</sub>/CB. (f) Wavelet transforms for the EXAFS of Ni-N<sub>x</sub>/CNS and Ni-N<sub>x</sub>/CB and reference samples. (g-h) The fitting curves of Fourier transformation of EXAFS spectra for Ni-N<sub>x</sub>/CNS and Ni-N<sub>x</sub>/CB, respectively.

(1.61 at%) and Ni contents (0.12 at%) compared to Ni-N<sub>x</sub>/CNS (C: 79.43 at%, N: 16.33 at%, Ni: 0.51 at%), which is consistent with the ICP-MS and elemental analyser results. The binding energies of Ni 2p<sub>3/2</sub> in Ni-N<sub>x</sub>/CNS and Ni-N<sub>x</sub>/CB were around 855.22 and 855.62 eV, respectively (Fig. 3a), which are higher than that of Ni metal (853.5 eV), implying the positive oxidation states of Ni single atoms [45]. As compared to Ni-N<sub>x</sub>/CNS, the binding energy of Ni 2p for Ni-N<sub>x</sub>/CB suggested a positive shift of ~0.4 eV, indicating that electrons may transfer from Ni atom to carbon black, thus exhibiting a more positive state. The N 1s high-resolution spectrum can be deconvoluted into five peaks corresponding to pyridinic N, Ni-N, pyrrolic N, quaternary N, and oxidized N at ~398.3, ~398.8, ~400.6, ~401.3, and ~403.0 eV, respectively (Fig. 3b) [45,46]. The contents of different N species in Ni-N<sub>x</sub>/CNS and Ni-N<sub>x</sub>/CB catalysts were also compared according to XPS results (Fig. 3c). In contrast to Ni-N<sub>x</sub>/CNS, the proportion of Ni-N increased and pyridinic N decreased while other N species remained

almost unchanged. This result indicated that although Ni-N<sub>x</sub>/CNS owned higher N content, the proportion of N dopants for coordinating with Ni was quite low compared to Ni-N<sub>x</sub>/CB.

X-ray absorption near-edge spectroscopy (XANES) and extended X-ray absorption fine structure (EXAFS) were applied to determine the coordination environment of the single-Ni-atoms in Ni-N<sub>x</sub>/CNS and Ni-N<sub>x</sub>/CB. The Ni K-edge XANES spectra for Ni-N<sub>x</sub>/CNS and Ni-N<sub>x</sub>/CB are apparently distinct from those of Ni foil and NiO references, where the Ni absorption edge position is between Ni foil and NiO, indicating a valence state between 0 ~ + 2 for Ni atoms, which is in consistency with the XPS results (Fig. 3d). The Fourier transform (FT) of EXAFS for Ni-N<sub>x</sub>/CNS and Ni-N<sub>x</sub>/CB and reference samples shown in Fig. 3e suggested Ni-N<sub>x</sub>/CNS and Ni-N<sub>x</sub>/CB both displayed a major peak at ~1.38 Å assigned to Ni-N bond, while the Ni-Ni peak at ~2.17 Å in Ni foil and Ni-O peak at ~1.68 Å in NiO was not detected in the spectra of both Ni-N<sub>x</sub>/CNS and Ni-N<sub>x</sub>/CB. Furthermore, wavelet transform (WT) for EXAFS was

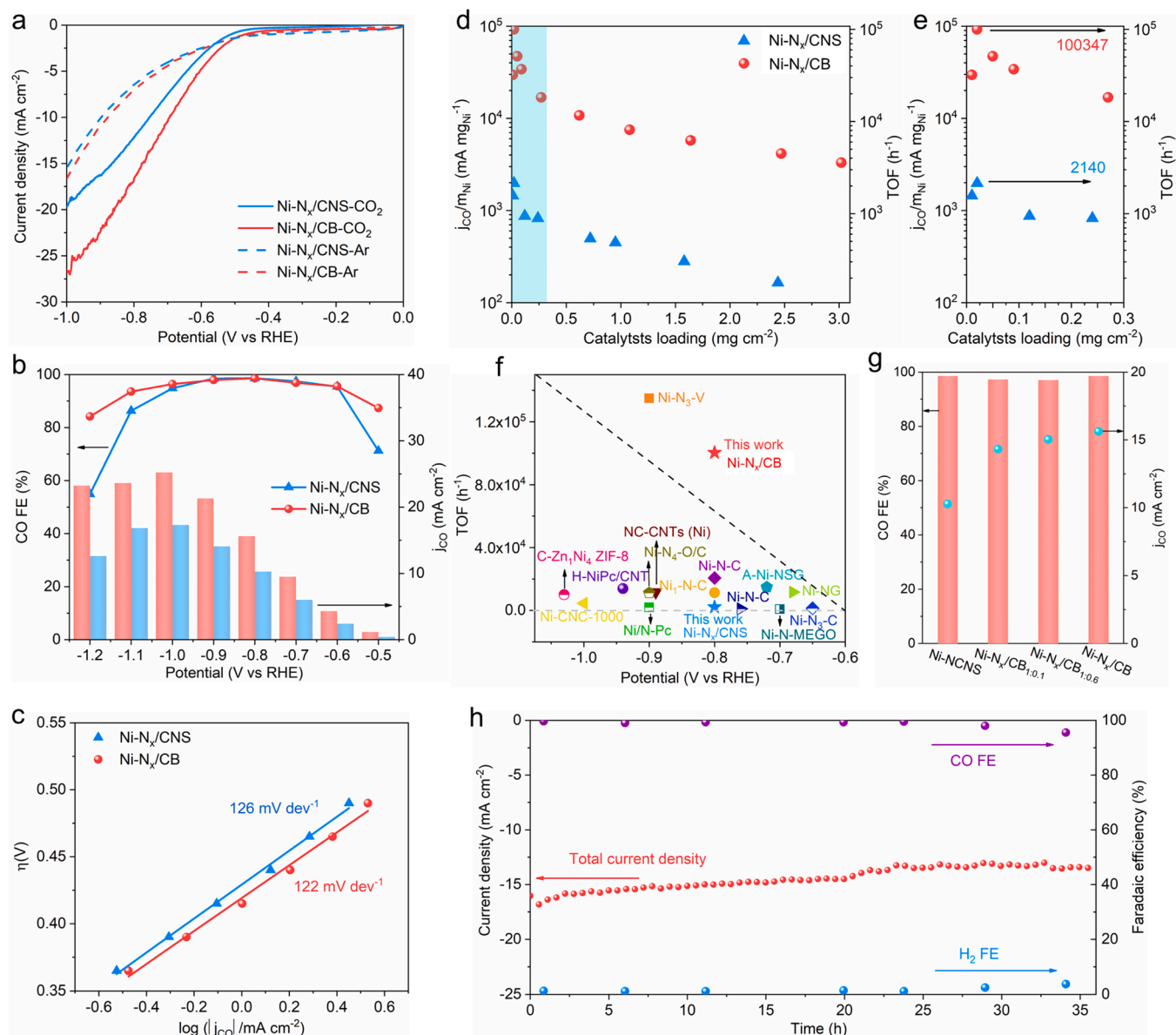


**Fig. 4.** CO<sub>2</sub>RR performances of different catalysts in H-type cell. (a) LSV curves in the Ar-saturated and CO<sub>2</sub>-saturated 0.5 M KHCO<sub>3</sub> electrolyte. (b) CO FEs and j<sub>CO</sub> at different applied potentials for Ni-N<sub>x</sub>/CNS and Ni-N<sub>x</sub>/CB with catalyst loading of ~1.5 mg cm<sup>-2</sup>. (c) Tafel slopes for CO production of Ni-N<sub>x</sub>/CNS and Ni-N<sub>x</sub>/CB. (d) Ni mass activities for CO formation and the corresponding TOF of Ni-N<sub>x</sub>/CNS and Ni-N<sub>x</sub>/CB. (e) Enlarged region (catalyst loading: 0 ~ 0.3 mg cm<sup>-2</sup>) of (d). (f) TOF of Ni-N<sub>x</sub>/CB compared with those of other previously reported single-Ni-atom catalysts for CO production (Table S2 for details). (g) CO FEs and j<sub>CO</sub> at -0.8 V vs. RHE for Ni-N<sub>x</sub>/CB<sub>1:x</sub> with different weight ratios of guanine to carbon black (1:0.1, 1:0.6, 1:2). (h) Long-term electrolysis of Ni-N<sub>x</sub>/CB at -0.8 V vs. RHE.

performed to intuitively show the types of coordination atoms (Fig. 3f). Ni-N<sub>x</sub>/CNS and Ni-N<sub>x</sub>/CB exhibited only one intensity maximum at  $\approx 4.0 \text{ \AA}^{-1}$ , which belonged to the Ni-N contributions, and the intensity maximum belonged to Ni-Ni bonds at  $\approx 7.0 \text{ \AA}^{-1}$  was absent, proving Ni atoms were atomically dispersed. To further analyze the coordination environment, EXAFS fittings for Ni-N<sub>x</sub>/CNS and Ni-N<sub>x</sub>/CB were performed. As illustrated in Fig. 3g-h and Fig. S9, the k space and R space matched well with the experimental curves. According to the fitting results (Table S1), the coordination number of the central Ni atom to N atoms was estimated to be 4.2 and 3.8 for Ni-N<sub>x</sub>/CNS and Ni-N<sub>x</sub>/CB, respectively, which are both close to the theoretical coordination number of 4. These results further confirmed the existence of single Ni-N<sub>x</sub> sites in Ni-N<sub>x</sub>/CNS and Ni-N<sub>x</sub>/CB catalysts.

### 3.2. Electrochemical CO<sub>2</sub> reduction and TOF calculation in H-type cell

The electrochemical CO<sub>2</sub>RR performance of catalysts was comparatively measured in an H-type cell containing CO<sub>2</sub>-saturated 0.5 M KHCO<sub>3</sub> electrolyte. LSV tests were first performed in Ar-saturated electrolyte and CO<sub>2</sub>-saturated electrolyte to assess the electrocatalytic activity of studied electrocatalysts (Fig. 4a). Ni-N<sub>x</sub>/CB and Ni-N<sub>x</sub>/CNS catalysts presented larger current densities in CO<sub>2</sub>-saturated electrolyte than in Ar-saturated electrolyte, indicating favorable CO<sub>2</sub>RR on these two catalysts. Besides, Ni-N<sub>x</sub>/CB suggested higher current density ( $26.7 \text{ mA cm}^{-2}$  at  $-1.0 \text{ V}$  vs. RHE) than Ni-N<sub>x</sub>/CNS ( $19.6 \text{ mA cm}^{-2}$ ), implying that Ni-N<sub>x</sub>/CB is more active for the CO<sub>2</sub>RR.

Subsequently, constant electrolysis at the potential range of  $-0.5 \sim -1.2 \text{ V}$  vs. RHE was carried out to analyze product selectivity and catalytic activity. The gas products were detected by online gas chromatographic (GC) equipment and no liquid products were found. After introducing carbon black support, Ni-N<sub>x</sub>/CB with lower Ni content (0.16 wt%) reversely showed an improved total current density as compared to Ni-N<sub>x</sub>/CNS with higher Ni content (2.42 wt%), which is consistent with the LSV result (Fig. S10). As for the product distribution shown in Fig. 4b and Fig. S11–12, only CO and H<sub>2</sub> were detected for all samples and their sum reached approximately 100%. Ni-N<sub>x</sub>/CB and Ni-N<sub>x</sub>/CNS catalysts both achieved high CO FEs over 95 % during the wide potential range from  $-0.6 \text{ V}$  to  $-1.0 \text{ V}$  vs. RHE and reached maximum CO FEs approaching 99 % at  $-0.8 \text{ V}$ . In comparison, Ni-N<sub>x</sub>/CB suggested higher CO FE at relatively negative potentials ( $-1 \sim -1.2 \text{ V}$  vs. RHE) than Ni-N<sub>x</sub>/CNS, which can be due to the presence of more unfavorable N species that promote the competitive HER under relatively negative potential [47]. Consequently, Ni-N<sub>x</sub>/CB reached a maximum CO partial current density ( $j_{\text{CO}}$ ) of  $25.2 \text{ mA cm}^{-2}$  at  $-1.0 \text{ V}$  vs. RHE, and achieved  $23.3 \text{ mA cm}^{-2}$  at  $-1.2 \text{ V}$ , which is 1.85 times that of Ni-N<sub>x</sub>/CNS under the same potential ( $12.6 \text{ mA cm}^{-2}$ ). For comparison, metal-free NCNS and NCB suggested lower CO selectivity and  $j_{\text{CO}}$  during the whole potential range than Ni-N<sub>x</sub>/CNS and Ni-N<sub>x</sub>/CB (Fig. S12). NCNS and NCB exhibited weak activity for CO production, revealing that single Ni atoms played the critical role in reducing CO<sub>2</sub> to CO. Besides, to exclude the influence of Ni agglomerate, we further employed an acid leaching process (washed in 3 M HCl for 12 h) to remove the Ni agglomerate and compared the CO<sub>2</sub>RR performance of Ni-N<sub>x</sub>/CNS and Ni-N<sub>x</sub>/CB catalysts before and after acid leaching, which suggested similar CO FEs and partial current density (Fig. S13). These results further proved that the Ni single atoms were the real active site for CO<sub>2</sub>RR.

Since the electrical conductivity may also affect the electrocatalytic current density, the electrical conductivities of Ni-N<sub>x</sub>/CNS and Ni-N<sub>x</sub>/CB were measured through Kelvin Four-terminal sensing (Fig. S14). Ni-N<sub>x</sub>/CB suggested a considerably lower value of electrical conductivity than that of Ni-N<sub>x</sub>/CNS, revealing that the higher current density of Ni-N<sub>x</sub>/CB large possibly derived from more exposed active sites. Besides, the Tafel slopes for CO production of Ni-N<sub>x</sub>/CNS and Ni-N<sub>x</sub>/CB were determined to be 126 and 122 mV decade<sup>-1</sup>, respectively, suggesting the rate-determining step might be a first electron transfer to generate CO<sub>2</sub><sup>-</sup> or

a concerted proton-electron transfer to generate \*COOH (Fig. 4c) [48–50]. To further investigate the reaction kinetics of the CO<sub>2</sub>RR, EIS for different catalysts was measured. As shown in Fig. S15, Ni-N<sub>x</sub>/CB suggested a smaller semi-circular diameter than Ni-N<sub>x</sub>/CNS, NCB and NCNS, indicating it exhibited a lower charge-transfer resistance, thus accelerating the electron transfer for the reaction intermediate formation. In situ ATR-IR measurements were also performed to investigate the key intermediate during the CO<sub>2</sub>RR for Ni-N<sub>x</sub>/CB catalyst in Fig. S16. Two negative peaks at 2343 and 1640 cm<sup>-1</sup> were observed for Ni-N<sub>x</sub>/CB, which can be assigned to CO<sub>2</sub> and H<sub>2</sub>O assumption, respectively. Besides, the peaks at 2070 cm<sup>-1</sup> can be assigned to \*CO intermediate, which can further desorb to generate CO product [51].

At present, most calculations on the amount of active sites for single-atom catalysts are still on the basis of the total mass loaded on the electrode. Many reported single-atom Ni catalysts with similar coordination environments have orders of magnitude differences in the CO<sub>2</sub>RR TOF value under approximate applied potentials, which may be largely caused by the calculation deviation of the amount of active sites rather than the intrinsic activity of active sites [45, 52–54]. In most research, the amount of active sites is overestimated because not all single-atom sites on the electrode are involved in the reaction, resulting in an underestimation of the TOF value. Due to the importance of the determination of the amount of active sites for TOF calculation, electrodes with different catalyst loading were prepared to find out the lowest catalyst loading that can ensure all supported catalysts are involved in electrocatalytic CO<sub>2</sub> reduction for TOF measurement. As illustrated in Fig. S17a, the CO partial current density first increased significantly with the increase of catalysts loading ( $0 \sim 1 \text{ mg cm}^{-2}$ ), then basically remained steady for both Ni-N<sub>x</sub>/CNS and Ni-N<sub>x</sub>/CB under the applied potential of  $-0.8 \text{ V}$ . As the catalyst loading is  $0.01 \text{ mg cm}^{-2}$ , the CO selectivity for both two catalysts are around 60 %, which may be because the catalyst does not completely cover the carbon paper, while as the catalyst loading increased to  $0.02 \text{ mg cm}^{-2}$ , the CO selectivity reached over 80 % (Fig. S17b). The Ni mass activity and the corresponding TOF were then calculated based on the  $j_{\text{CO}}$  and catalyst loading (Fig. 4d-e). The calculation of Ni mass activity and the corresponding TOF for both Ni-N<sub>x</sub>/CNS and Ni-N<sub>x</sub>/CB catalysts reached the maximum value under a catalyst loading of  $0.02 \text{ mg cm}^{-2}$ , and then as the loading increased beyond  $0.02 \text{ mg cm}^{-2}$ , Ni mass activity and TOF decreased gradually since the amount of active sites was overestimated. Consequently, the catalyst loading of  $0.02 \text{ mg cm}^{-2}$  is considered to be a suitable loading that can ensure all loaded catalysts participate in the reduction reaction for accurate TOF calculation. The amount of Ni sites over Ni-N<sub>x</sub>/CNS and Ni-N<sub>x</sub>/CB was calculated to be  $0.484 \mu\text{g/cm}^2$  and  $0.032 \mu\text{g/cm}^2$ , respectively.

As shown in Fig. 4e, the TOF of Ni-N<sub>x</sub>/CB for CO production was then calculated to be  $100347 \text{ h}^{-1}$  at  $-0.8 \text{ V}$ , which is significantly higher than that of Ni-N<sub>x</sub>/CNS ( $2140 \text{ h}^{-1}$  at  $-0.8 \text{ V}$ ) and other previously reported single-Ni-atom catalysts (Fig. 4f and Table S2). Notably, the order of magnitude differences exists in the  $j_{\text{CO}}$  of single-Ni-atom catalysts in different reports, but such difference is largely due to the calculation deviation of the amount of active sites (Table S2). For example, the CO partial current density of Ni-N<sub>3</sub>-V ( $47.5 \text{ mA cm}^{-2}$ ) [55] is only  $\sim 1.4$  times that of Ni/N-Pc ( $33 \text{ mA cm}^{-2}$ ) [53] under  $-0.9 \text{ V}$  vs. RHE, while the taken number of active sites ( $0.48 \mu\text{g cm}^{-2}$  of Ni) is much smaller than that of Ni/N-Pc ( $1 \text{ mg cm}^{-2} \times 1.69 \text{ wt\%} = 16.9 \mu\text{g cm}^{-2}$  of Ni), so that the calculated TOF values suggest a gap of two orders of magnitude ( $13,500 \text{ h}^{-1}$  with respect to  $2029 \text{ h}^{-1}$ ). Therefore, the utilization of active sites varies widely even for single-atom catalysts. The Ni content in most reported single-Ni-atom catalysts shown in Table S2 is between 1  $\sim$  3 wt%, and the TOF normally ranges from 1000 to 30,000 under the potential of  $-0.7 \sim -1.0 \text{ V}$ . While for the as-prepared Ni-N<sub>x</sub>/CB, low Ni content (0.16 wt%), as well as low electrode loading ( $0.02 \text{ mg cm}^{-2}$ ) reached a  $j_{\text{CO}}$  up to  $3 \text{ mA cm}^{-2}$  at  $-0.8 \text{ V}$ . Therefore, the ultrahigh CO TOF for Ni-N<sub>x</sub>/CB can be attributed to the high intrinsic activity as well as high utilization of single Ni atoms on the electrode.



Within Ni-N<sub>x</sub>/CNS, abundant Ni-N sites were buried in the carbon nanosheets, which were not accessible to the reactants. While after introducing carbon black, the bulk guanine absorbed with Ni<sup>2+</sup> ions was gradually merged into the surface of carbon black nanoparticles (SEM images of Fig. S18), consequently, Ni-N sites tend to be formed over the surface of carbon black particles during pyrolysis, leading to high accessibility to reactants. This also reminds us to pay attention to the catalyst loading on the electrode when conducting experiments for TOF calculation, and strive to develop a more accurate approach for quantifying the amount of surficial active sites.

To reveal the effect of the introduction of carbon black on improving the utilization of single atoms over the carbon matrix, Ni-N<sub>x</sub>/CB<sub>1:x</sub> with different weight ratios of guanine to carbon black (1:0.1, 1:0.6, 1:2) were comparatively applied for CO<sub>2</sub>RR, in which the Ni content was detected to be 1.72 wt%, 0.51 wt%, 0.16 wt%, and 0.11 wt%, respectively. No metallic peak assigned to Ni<sup>0</sup> was observed in the XRD graph for all samples (Fig. S19). As shown in Fig. 4f, Ni-N<sub>x</sub>/CB<sub>1:x</sub> with different weight ratios of guanine to carbon black all exhibited high CO FEs of 96~99% at -0.8 V (98.6 %, 97.2 %, 97.0 %, 98.6 %, and 96.4 %, respectively) and similar *j*<sub>CO</sub> of around 15 mA cm<sup>-2</sup>. TOF calculation of Ni-N<sub>x</sub>/CB<sub>1:x</sub> samples with catalysts loading of 0.02 mg cm<sup>-2</sup> for CO production was also conducted under the potential of -0.8 V (Fig. S20). Ni-N<sub>x</sub>/CB<sub>1:0.1</sub>, Ni-N<sub>x</sub>/CB<sub>1:0.6</sub>, and Ni-N<sub>x</sub>/CB with similar CO partial current density exhibited totally distinct TOF values: 8619, 41,054, and 100,347 h<sup>-1</sup>, respectively, which were correlated to the quantification of active sites on the electrode. The SEM images (Fig. S21) suggested that carbon black nanoparticles and carbon nanosheets coexisted in Ni-N<sub>x</sub>/CB<sub>1:0.1</sub> and Ni-N<sub>x</sub>/CB<sub>1:0.6</sub> catalysts, revealing that some single Ni atoms were still embodied in the carbon sheet. Therefore, a large amount of single Ni atoms cannot participate in CO<sub>2</sub>RR. In contrast, Ni-N<sub>x</sub>/CB showing dominant spherical particle morphology reached high utilization of single Ni atoms, thus it exhibited the highest TOF value. In addition, to exclude the influence of large differences in Ni content in catalysts on TOF calculation, we also prepared Ni-N<sub>x</sub>/CNS-*x* wt% with lower Ni content close to that of Ni-N<sub>x</sub>/CB (0.12 wt% and 0.22 wt%, respectively) for CO<sub>2</sub>RR, and compare them with Ni-N<sub>x</sub>/CB. As shown in Fig. S22, they both suggested lower CO FE, partial current density and TOF value than Ni-N<sub>x</sub>/CB, which further supported the high utilization of single Ni atoms in Ni-N<sub>x</sub>/CB as compared to Ni-N<sub>x</sub>/CNS catalysts.

Ni-N<sub>x</sub>/CB prepared with another two commercial carbon blacks (Ketjenblack ECP600JD, Cabot BP-2000) with higher specific surface areas around 1400 m<sup>2</sup> g<sup>-1</sup> using the same procedure also presented high CO selectivity over 90% during a wide potential range from -0.6 to -1.2 V vs. RHE and high activity (Fig. S23). This result indicated that carbon black with various specific surface areas exhibited different optimal weight ratios of guanine to carbon black in terms of CO partial current density, but they all achieved high CO selectivity over 90 %.

Furthermore, maintaining the amount of guanine and carbon black unchanged, Ni-N<sub>x</sub>/CB-*x* wt% catalysts with different additions of Ni precursor were also prepared for CO<sub>2</sub> electroreduction (Fig. S24). Ni-N<sub>x</sub>/CB-0.16 wt% with a Ni content of 0.16 wt% reached both relatively higher CO selectivity and CO partial current density than Ni-N<sub>x</sub>/CB-0.07 wt% and Ni-N<sub>x</sub>/CB-0.77 wt%. The lower activity of Ni-N<sub>x</sub>/CB-0.07 wt% could be attributed to the lower amount of single Ni atoms, while for Ni-N<sub>x</sub>/CB-0.77 wt%, the relatively low *j*<sub>CO</sub> might be due to the formation of small Ni nanoparticles or Ni nanoclusters.

Ni-N<sub>x</sub>/CB prepared on a larger scale (the amount of precursors was 6 times the usual amount) with ~12.7 g catalysts obtained was also applied for CO<sub>2</sub> electroreduction to investigate the scalability of the preparation approach, which suggested a similar performance to the usual one (Fig. S25), confirming the scalability of this synthesis method. In addition, Ni-N<sub>x</sub>/CB maintained a relatively steady current density with a CO FE over 90 % during long-term electrolysis of 36 h at -0.8 V vs. RHE without obvious decline, demonstrating an excellent stability of Ni-N<sub>x</sub>/CB during CO<sub>2</sub>RR, which is superior to most reported single-Ni-atom catalysts (Fig. 4h, Fig. S26, and Table S2).

Based on all the above results, Ni-N<sub>x</sub>/CNS and a series of Ni-N<sub>x</sub>/CB catalysts all suggest high CO selectivity up to > 97 %. The product selectivity mostly depends on the intrinsic activity of the active site. As we have summarized in our previous review [32], Ni with distinct coordination environments (including Ni-N<sub>3</sub>, Ni-N<sub>4</sub>, Ni-N<sub>x</sub>C<sub>4-x</sub> (*x* = 1–3) and coordinatively unsaturated Ni-N sites) reported by different groups all show high CO selectivity (mostly can reach more than 95 %). Therefore, all Ni-N<sub>x</sub> sites with different coordination environments exhibit very similar intrinsic activity for CO production. In contrast, the catalyst activity (current density) is closely related to the number of active sites participating in the reaction. We infer that the superior activity of Ni-N<sub>x</sub>/CB to Ni-N<sub>x</sub>/CNS can be mainly attributed to more exposed and accessible Ni-N<sub>x</sub> sites on the carbon black surface.

### 3.3. Electrochemical CO<sub>2</sub> reduction in flow cell

Because of the low solubility of CO<sub>2</sub> in the KHCO<sub>3</sub> electrolyte, the total current density was significantly limited in the H-type cell. Therefore, gas diffusion electrodes supporting Ni-N<sub>x</sub>/CB and Ni-N<sub>x</sub>/CNS catalysts were employed within a flow cell, where gaseous CO<sub>2</sub> can be directly transferred into the catalyst surface to establish a three-phase interface (Fig. 5a). As displayed in Fig. 5b, the total current density of both Ni-N<sub>x</sub>/CNS and Ni-N<sub>x</sub>/CB catalysts in the flow cell is much higher than that in the H-type cell, proving the superiority of such flow cell configuration. The resistance values (*R*<sub>s</sub>) were 4.0 Ohms for Ni-N<sub>x</sub>/CB and 4.2 Ohms for Ni-N<sub>x</sub>/CNS fitted from the EIS data. After manual *iR*<sub>s</sub> correction, Ni-N<sub>x</sub>/CB and Ni-N<sub>x</sub>/CNS achieved remarkable total current densities of 195 and 183 mA cm<sup>-2</sup> at extremely low potentials of -0.42 and -0.43 V vs RHE, respectively. Notably, the Ni-N<sub>x</sub>/CB catalyst with lower Ni single-atom loading suggested higher activity than Ni-N<sub>x</sub>/CNS as in the H-type cell. Besides, during the potential range of -0.3 ~ -0.45 V vs RHE, Ni-N<sub>x</sub>/CB and Ni-N<sub>x</sub>/CNS both reached a maximum CO selectivity approaching 100%. Ni-N<sub>x</sub>/CB and Ni-N<sub>x</sub>/CNS also displayed high CO FE of ~100 % as well as superior current density up to 238.7 mA cm<sup>-2</sup> and 206.3 mA cm<sup>-2</sup> at -0.8 V vs RHE with automatic IR correction in the flow cell, which is 15.1 and 19.8 times higher than those in the H-type cell, respectively (Fig. S27), demonstrating the outperforming performance of Ni-N<sub>x</sub>/CB and Ni-N<sub>x</sub>/CNS in the gas diffusion system.

Furthermore, to realize the industrial application of CO<sub>2</sub>RR, we further tested the performance of the Ni-N<sub>x</sub>/CB-large (prepared on large scale) catalyst in the flow cell by the galvanostatic method under 100, 200, 300, 400, and 500 mA cm<sup>-2</sup> (Fig. 5e, Table S3). A maximum CO FE approaching 100 % was also observed for Ni-N<sub>x</sub>/CB-large under 100 ~ 300 mA cm<sup>-2</sup>, and the catalyst achieved a superior *j*<sub>CO</sub> up to ~ 450 mA cm<sup>-2</sup> in the flow cell configuration, which presented outstanding efficiency in CO production as compared to state-of-the-art Ni single-atom electrocatalysts reported previously (Table S4). Moreover, it maintained well CO selectivity over 98% under 100 mA cm<sup>-2</sup> during 11 h of the electrolysis, and maintained CO FE over 95 % under 300 mA cm<sup>-2</sup> during 3 h of the electrolysis (Fig. 5f and Fig. S28). But the potential keeps rising due to the decline of electrode hydrophobicity and the caused flooding, which need to be further improved. The XRD, TEM and STEM results (Fig. S29) of the sample after long-term electrolysis revealed that no Ni nanoparticles were formed during the long-term reaction.

### 3.4. Rechargeable Zn-CO<sub>2</sub> electrochemical cell

Since Ni-N<sub>x</sub>/CB has suggested superior performance for CO<sub>2</sub> electroreduction to CO, the Zn-CO<sub>2</sub> battery test was further performed with Ni-N<sub>x</sub>/CB as cathode and Zn plate as anode (Fig. 6a) [56]. During the discharge process, CO<sub>2</sub>RR proceeds over the cathode catalyst and the anodic Zn plate is dissolved into the electrolyte. While during the charge process, oxygen evolution reaction occurs on the cathode and Zn<sup>2+</sup> ions are reduced. The discharge-charge voltage profiles shown in Fig. 5b

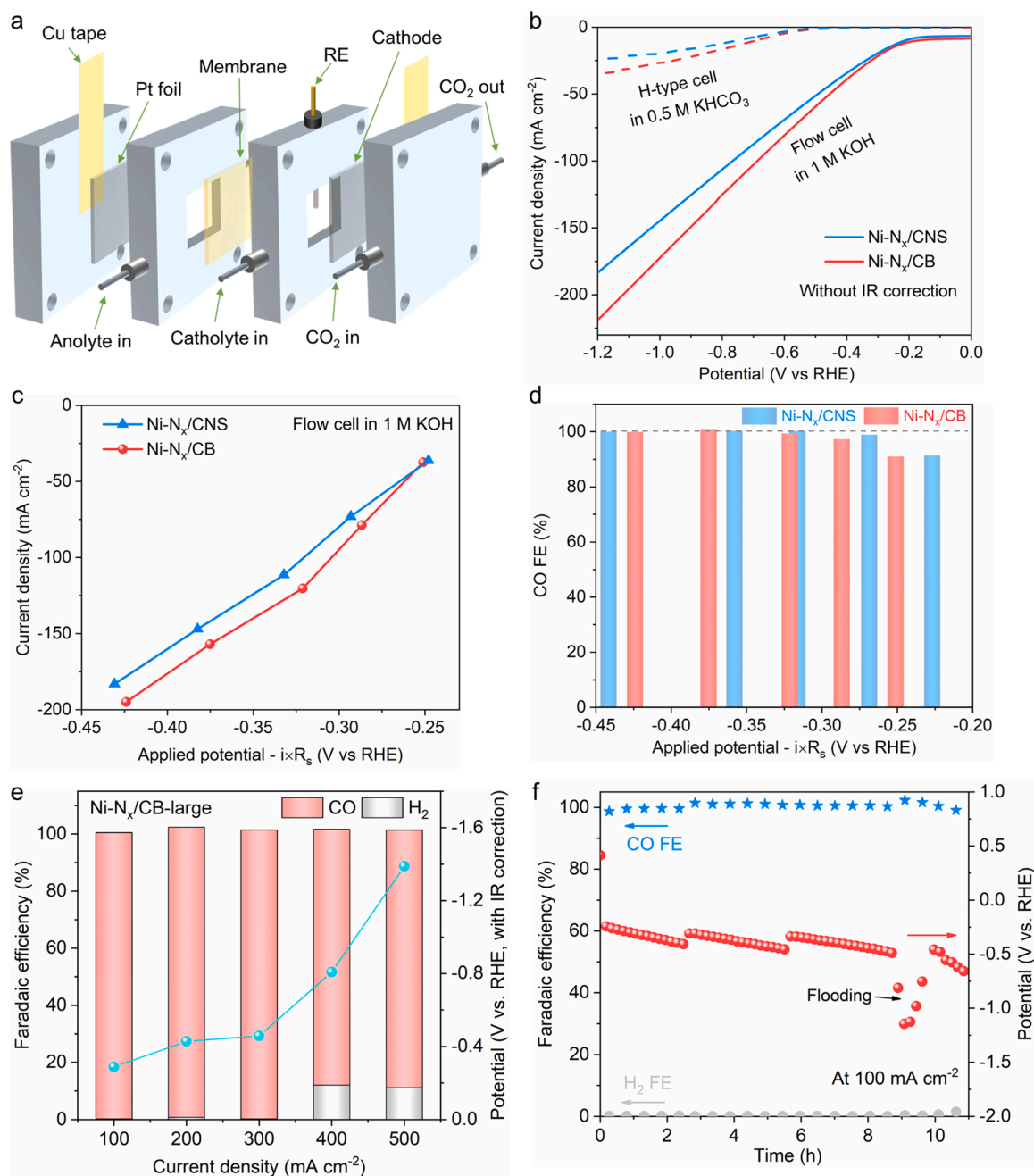


**Fig. 5.** CO<sub>2</sub>RR performances of different catalysts in the flow cell. (a) Schematic illustration of the flow cell. (b) LSV curves for Ni-N<sub>x</sub>/CB and Ni-N<sub>x</sub>/CNS in 1 M KOH electrolyte within flow cell configuration compared with that in 0.5 M KHCO<sub>3</sub> electrolyte within H-type cell. (c) Current densities and (d) CO FEs at different applied potentials with manual IR correction for Ni-N<sub>x</sub>/CNS and Ni-N<sub>x</sub>/CB in 1 M KOH within the flow cell. (e) CO FEs and potential (vs. RHE, with IR correction) at different current densities for Ni-N<sub>x</sub>/CB-large in 1 M KOH. (f) Long-term electrolysis of Ni-N<sub>x</sub>/CB-large under 100 mA cm<sup>-2</sup>.

indicated the rechargeable property of the Zn-CO<sub>2</sub> battery, and it reached the peak power density of 0.96 mW cm<sup>-2</sup> at 1.58 mA cm<sup>-2</sup> during the discharge process. Three Zn-CO<sub>2</sub> batteries with Ni-N<sub>x</sub>/CB as cathode in series are able to light up light-emitting diodes, demonstrating efficient energy output of the Zn-CO<sub>2</sub> battery. (Fig. 6c). In addition, the CO selectivity under constant discharge current densities of 0.5 ~ 3 mA cm<sup>-2</sup> was detected (Fig. 6d). The CO FE reached a maximum value up to 75 % at the discharge current density of 2 mA cm<sup>-2</sup>, indicating the efficient performance of Ni-N<sub>x</sub>/CB for CO<sub>2</sub>RR. However, the CO selectivity and the current density are still lower than the CO<sub>2</sub>RR performed in the H-type cell and flow cell, which need to be further improved (Table S5). Furthermore, the discharge-recharge cycles under a constant current density of 1 mA cm<sup>-2</sup> for Ni-N<sub>x</sub>/CB suggested a stable

voltage gap of 1.5 V during 36 cycles for 12 h (Fig. S30), indicating good durability of the Zn-CO<sub>2</sub> battery.

#### 4. Conclusion and prospect

In summary, two Ni, N-doped carbon catalysts (Ni-N<sub>x</sub>/CB and Ni-N<sub>x</sub>/CNS) were synthesized by a facile one-step pyrolysis strategy. The combination of the XAS and HAADF-STEM technologies confirmed the formation of atomically dispersed Ni-N<sub>x</sub> moieties on the carbon nanosheet or carbon black for Ni-N<sub>x</sub>/CNS and Ni-N<sub>x</sub>/CB, respectively. In Ni-N<sub>x</sub>/CNS, the morphology of 2D nanosheets leads to the embedding of a large amount of single-Ni-atom sites. While after introducing carbon black, although the obtained Ni-N<sub>x</sub>/CB catalyst suggested a reduced

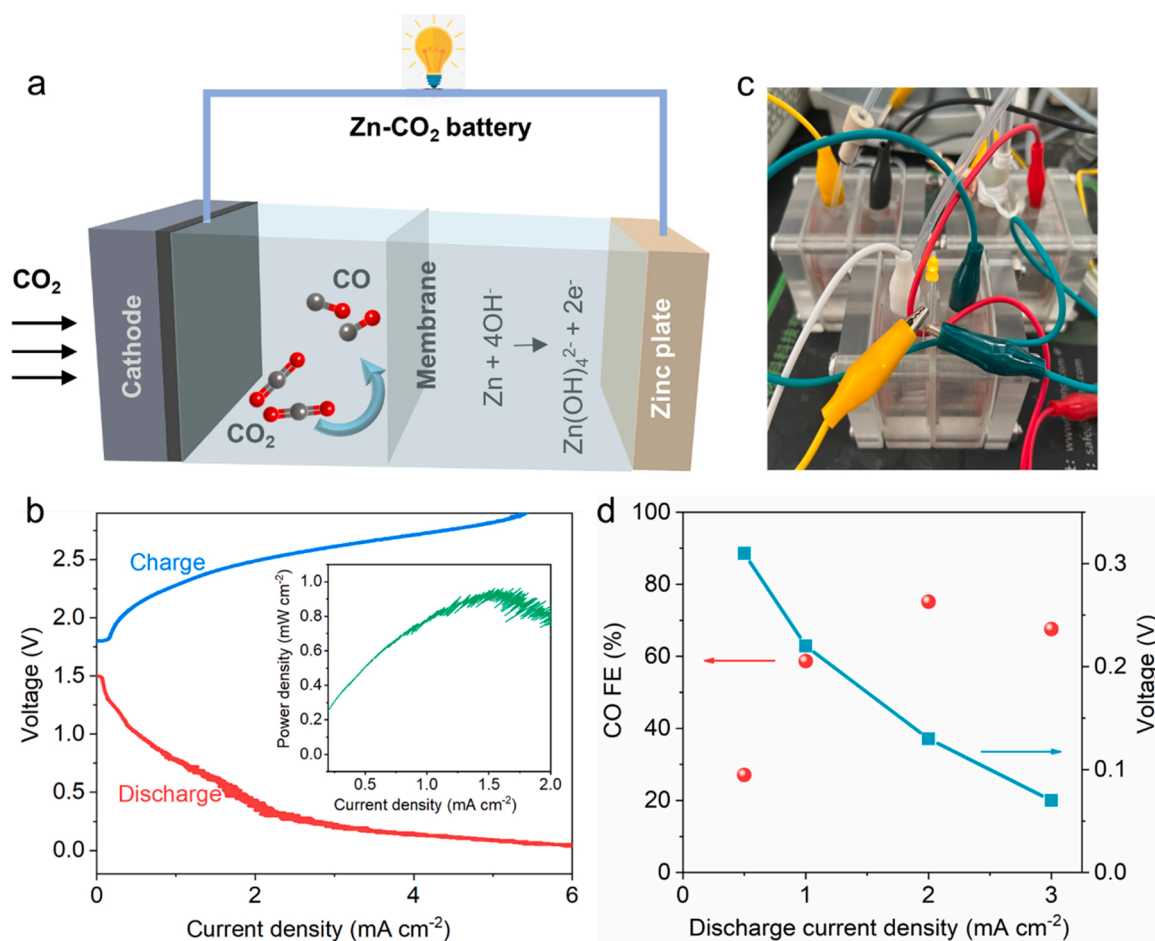


**Fig. 6.** The rechargeable Zn-CO<sub>2</sub> electrochemical cell. (a) Schematic diagram for Zn-CO<sub>2</sub> battery. (b) Charge-discharge polarization and power density curves. (c) Photo displaying the light-emitting diodes powered by three Zn-CO<sub>2</sub> batteries in series. (d) Discharge curves at different current densities and CO FE.

single-Ni-atom loading from 2.42 wt% to 0.16 wt%, more accessible single-Ni-sites dispersed over the surface to the reactants were presented, thus the utilization of single-Ni-atom was greatly improved. This in turn leads to the superior catalytic performance of the Ni-N<sub>x</sub>/CB for CO<sub>2</sub>RR in contrast to Ni-N<sub>x</sub>/CNS. Consequently, the Ni-N<sub>x</sub>/CB catalyst not only employed commercial carbon black as support to increase catalysts yield, but also exhibited high CO FE over 90% during a wide potential window from -0.6 to -1.1 V vs RHE and achieved higher CO partial current densities than Ni-N<sub>x</sub>/CNS during the whole selected potential range. Particularly, an ultrahigh TOF value of 100347 h<sup>-1</sup> was achieved for Ni-N<sub>x</sub>/CB under -0.8 V, which is approximately ten times higher than the literature reports. In addition, a remarkable CO partial current density up to 300 mA cm<sup>-2</sup> with a nearly 100% CO FE was achieved in the flow cell system, and the assembled Zn-CO<sub>2</sub> battery with Ni-N<sub>x</sub>/CB as cathode presented the capability of energy output with good stability. The present result in this work reminds the importance of maximizing the utilization of active sites in single-atom catalysts, which would inspire the development of single-atom carbon-based catalysts with unique structures to maximally expose active sites while increasing the loading to achieve high performance.

To fully utilize single-atom with high metal loading, it is necessary to avoid the agglomeration of atoms to form clusters or particles and avoid single-atom sites being buried in dense carbon frameworks or growing in inaccessible micropores. Design of open and unique structures with large specific surface areas such as three-dimensional structures, hollow structures, and mesoporous structures can be considered to increase the exposure of single atoms and promote the dispersion of single atoms. On the other hand, it is also necessary to reduce the pyrolysis temperature

as much as possible to avoid agglomeration or to develop methods for preparing single-atom catalysts at room temperature or low temperature. In short, it is significant to balance the improvement of active site exposure as well as active site loading for single-atom catalysts.

#### CRediT authorship contribution statement

**Shuyu Liang:** Methodology, Investigation, Validation, Formal analysis, Writing - original draft. **Tianyu Zhang:** Supervision, Conceptualization, Discussion, Writing-Reviewing and Editing. **Yue Zheng:** Supporting Methodology, Validation. **Tianshan Xue:** Supporting Methodology, Investigation. **Zheng Wang:** Writing-Reviewing and Editing. **Qiang Wang:** Supervision, Conceptualization, Discussion, Writing-Reviewing and Editing, Funding acquisition. **Hong He:** Supervision, Conceptualization, Discussion, Writing- Reviewing and Editing.

#### Declaration of Competing Interest

The authors declare that they have no known competing financial interests or personal relationships that could have appeared to influence the work reported in this paper.

#### Data availability

Data will be made available on request.



## Acknowledgments

This work was supported by the National Natural Science Foundation of China (52225003, 22208021), the Beijing Municipal Education Commission through the Innovative Transdisciplinary Program “Ecological Restoration Engineering”.

## Appendix A. Supporting information

Supplementary data associated with this article can be found in the online version at [doi:10.1016/j.apcatb.2023.122801](https://doi.org/10.1016/j.apcatb.2023.122801).

## References

- [1] Y.Y. Birdja, E. Pérez-Gallent, M.C. Figueiredo, A.J. Göttele, F. Calle-Vallejo, M.T. M. Koper, Advances and challenges in understanding the electrocatalytic conversion of carbon dioxide to fuels, *Nat. Energy* 4 (2019) 732–745, <https://doi.org/10.1038/s41560-019-0450-y>.
- [2] Chang Yu Xinyi Tan, Song Cui Yongwen Ren, J.Qiu Wenbin Lia, Recent advance in innovative strategies for CO<sub>2</sub> electroreduction reaction, *Energy Environ. Sci.* 14 (2021) 765–780, <https://doi.org/10.1039/D0EE02981E>.
- [3] R.I. Masel, Z.C. Liu, H.Z. Yang, J.J. Kaczur, D. Carrillo, S.X. Ren, D. Salvatore, C. P. Berlinguette, An industrial perspective on catalysts for low-temperature CO<sub>2</sub> electrolysis, *Nat. Nanotechnol.* 16 (2021) 118–128, <https://doi.org/10.1038/s41565-020-00823-x>.
- [4] Z. Liang, L. Song, M. Sun, B. Huang, Y. Du, Tunable CO/H<sub>2</sub> ratios of electrochemical reduction of CO<sub>2</sub> through the Zn-Ln dual atomic catalysts. *Sci. Adv.* 7 (2021), eabl4915 <https://doi.org/10.1126/sciadv.abl4915>.
- [5] Y. Pan, R. Lin, Y. Chen, S. Liu, W. Zhu, X. Cao, W. Chen, K. Wu, W.C. Cheong, Y. Wang, L. Zheng, F. Luo, Y. Lin, Y. Liu, C. Liu, J. Li, Q. Lu, X. Chen, D. Wang, Q. Peng, C. Chen, Y. Li, Design of single-atom Co-N<sub>5</sub> catalytic site: A robust electrocatalyst for CO<sub>2</sub> reduction with nearly 100% CO selectivity and remarkable stability, *J. Am. Chem. Soc.* 140 (2018) 4218–4221, <https://doi.org/10.1021/jacs.8b00814>.
- [6] J.M. Strain, S. Gulati, S. Pishgar, J.M. Spurgeon, Pulsed electrochemical carbon monoxide reduction on oxide-derived copper catalyst, *ChemSusChem* 13 (2020) 3028–3033, <https://doi.org/10.1002/cssc.202000464>.
- [7] C.B. Lu, K.Y. Jiang, D. Trancan, N. Wang, H. Zhu, F. Rodriguez-Hernandez, Z. Y. Chen, C.Q. Yang, F. Zhang, Y.Z. Su, C.C. Ke, J.C. Zhang, Y. Han, X.D. Zhuang, Electrochemical reduction of carbon dioxide with nearly 100% carbon monoxide faradaic efficiency from vacancy-stabilized single-atom active sites, *J. Mater. Chem. A* 9 (2021) 24955–24962, <https://doi.org/10.1039/d1ta05990d>.
- [8] P. Zhai, Y.W. Li, M. Wang, J.J. Liu, Z. Cao, J. Zhang, Y. Xu, X.W. Liu, Y.W. Li, Q. J. Zhu, D.Q. Xiao, X.D. Wen, D. Ma, Development of direct conversion of syngas to unsaturated hydrocarbons based on Fischer-Tropsch route, *Chem* 7 (2021) 3027–3051, <https://doi.org/10.1016/j.chempr.2021.08.019>.
- [9] R.M. Navarro, M.A. Pena, J.L.G. Fierro, Hydrogen production reactions from carbon feedstocks: fossils fuels and biomass, *Chem. Rev.* 107 (2007) 3952–3991, <https://doi.org/10.1021/cr0501994>.
- [10] C. Xu, A. Vasileff, Y. Zheng, S.Z. Qiao, Recent progress of 3d transition metal single-atom catalysts for electrochemical CO<sub>2</sub> reduction, *Adv. Mater. Interfaces* 8 (2020), 2001904, <https://doi.org/10.1002/admi.202001904>.
- [11] A.S. Varela, W. Ju, A. Bagger, P. Franco, J. Rossmeisl, P. Strasser, Electrochemical reduction of CO<sub>2</sub> on metal-nitrogen-doped carbon catalysts, *ACS Catal.* 9 (2019) 7270–7284, <https://doi.org/10.1021/acscatal.9b01405>.
- [12] T. Hatsukade, K.P. Kuhl, E.R. Cave, D.N. Abram, T.F. Jaramillo, Insights into the electrocatalytic reduction of CO<sub>2</sub> on metallic silver surfaces, *Phys. Chem. Chem. Phys.* 16 (2014) 13814–13819, <https://doi.org/10.1039/c4cp00692e>.
- [13] Y. Chen, C.W. Li, M.W. Kanan, Aqueous CO<sub>2</sub> reduction at very low overpotential on oxide-derived Au nanoparticles, *J. Am. Chem. Soc.* 134 (2012) 19969–19972, <https://doi.org/10.1021/ja309317u>.
- [14] Q. Lu, J. Rosen, Y. Zhou, G.S. Hutchings, Y.C. Kimmel, J.G. Chen, F. Jiao, A selective and efficient electrocatalyst for carbon dioxide reduction, *Nat. Commun.* 5 (2014) 3242, <https://doi.org/10.1038/ncomms4242>.
- [15] D.A. Bulushev, A.D. Nishchakova, S.V. Trubina, O.A. Stonkus, I.P. Asanov, A. V. Okotrub, L.G. Bulusheva, Ni-N<sub>4</sub> sites in a single-atom Ni catalyst on N-doped carbon for hydrogen production from formic acid, *J. Catal.* 402 (2021) 264–274, <https://doi.org/10.1016/j.jcat.2021.08.044>.
- [16] E. Lepre, J. Heske, M. Nowakowski, E. Scoppola, I. Zizak, T. Heil, T.D. Kühne, M. Antonietti, N. López-Salas, J. Alberio, Ni-based electrocatalysts for unconventional CO<sub>2</sub> reduction reaction to formic acid, *Nano Energy* 97 (2022), <https://doi.org/10.1016/j.nanoen.2022.107191>.
- [17] T. Asset, S.T. Garcia, S. Herrera, N. Andersen, Y. Chen, E.J. Peterson, I. Matanovic, K. Artyushkova, J. Lee, S.D. Minter, S. Dai, X. Pan, K. Chavan, S. Calabrese Barton, P. Atanassov, Investigating the nature of the active sites for the CO<sub>2</sub> reduction reaction on carbon-based electrocatalysts, *ACS Catal.* 9 (2019) 7668–7678, <https://doi.org/10.1021/acscatal.9b01513>.
- [18] W. Ju, A. Bagger, G.P. Hao, A.S. Varela, I. Sinev, V. Bon, B. Roldan Cuenya, S. Kaskel, J. Rossmeisl, P. Strasser, Understanding activity and selectivity of metal-nitrogen-doped carbon catalysts for electrochemical reduction of CO<sub>2</sub>, *Nat. Commun.* 8 (2017) 944, <https://doi.org/10.1038/s41467-017-01035-z>.
- [19] L. Takele Menisa, P. Cheng, C. Long, X. Qiu, Y. Zheng, J. Han, Y. Zhang, Y. Gao, Z. Tang, Insight into atomically dispersed porous M-N-C single-site catalysts for electrochemical CO<sub>2</sub> reduction, *Nanoscale* 12 (2020) 16617–16626, <https://doi.org/10.1039/d0nr03044a>.
- [20] X. Sun, Y. Tuo, C. Ye, C. Chen, Q. Lu, G. Li, P. Jiang, S. Chen, P. Zhu, M. Ma, J. Zhang, J.H. Bitter, D. Wang, Y. Li, Phosphorus induced electron localization of single iron sites for boosted CO<sub>2</sub> electroreduction reaction, *Angew. Chem. Int. Ed.* 60 (2021) 23614–23618, <https://doi.org/10.1002/anie.202110433>.
- [21] Y. Li, X.F. Lu, S. Xi, D. Luan, X. Wang, X.W.D. Lou, Synthesis of N-doped highly graphitic carbon urchin-like hollow structures loaded with single-Ni Atoms towards efficient CO(2) electroreduction, *Angew. Chem. Int. Ed.* 61 (2022), e202201491, <https://doi.org/10.1002/anie.202201491>.
- [22] Y. Li, S.L. Zhang, W. Cheng, Y. Chen, D. Luan, S. Gao, X.W.D. Lou, Loading single-Ni atoms on assembled hollow N-rich carbon plates for efficient CO<sub>2</sub> electroreduction, *Adv. Mater.* 34 (2022), 2105204, <https://doi.org/10.1002/adma.202105204>.
- [23] F. Pan, W. Deng, C. Justiniano, Y. Li, Identification of champion transition metals centers in metal and nitrogen-codoped carbon catalysts for CO<sub>2</sub> reduction, *Appl. Catal. B* 226 (2018) 463–472, <https://doi.org/10.1016/j.apcatb.2018.01.001>.
- [24] H. Yang, L. Shang, Q. Zhang, R. Shi, G.I.N. Waterhouse, L. Gu, T. Zhang, A universal ligand mediated method for large scale synthesis of transition metal single atom catalysts, *Nat. Commun.* 10 (2019) 4585, <https://doi.org/10.1038/s41467-019-12510-0>.
- [25] Hui-Yun Jeong, Mani Balamurugan, Venkata Sury, Kumar Choutipalli, Eun-suk Jeong, Venkatesan Subramanian, U. Sim, K.T. Nam, Achieving highly efficient CO<sub>2</sub> to CO electroreduction exceeding 300 mA cm<sup>-2</sup> with single-atom nickel electrocatalysts, *J. Mater. Chem. A* 7 (2019) 10651–10661, doi: 10.1039/C9TA02405K.
- [26] Long Jiao, Weijie Yang, Gang Wan, Rui Zhang, Xusheng Zheng, Hua Zhou, Shu-Hong Yu, H.-L. Jiang, Single-atom electrocatalysts from multivariate metal-organic frameworks for highly selective reduction of CO<sub>2</sub> at low pressures, *Angew. Chem. Int. Ed.* 59 (2020) 20589–20595, <https://doi.org/10.1002/anie.202008787>.
- [27] C. Zhao, X. Dai, T. Yao, W. Chen, X. Wang, J. Wang, J. Yang, S. Wei, Y. Wu, Y. Li, Ionic exchange of metal-organic frameworks to access single nickel sites for efficient electroreduction of CO<sub>2</sub>, *J. Am. Chem. Soc.* 139 (2017) 8078–8081, <https://doi.org/10.1021/jacs.7b02736>.
- [28] Yun-Nan Gong, Long Jiao, Yunyang Qian, Chun-Yang Pan, Lirong Zheng, Xuechao Cai, Bo Liu, Shu-Hong Yu, H.-L. Jiang, Regulating the coordination environment of MOF-templated single-atom nickel electrocatalysts for boosting CO<sub>2</sub> reduction, *Angew. Chem. Int. Ed.* 59 (2020) 2705–2709, <https://doi.org/10.1002/ange.2020194977>.
- [29] Z. Chen, X. Zhang, W. Liu, M. Jiao, K. Mou, X. Zhang, L. Liu, Amination strategy to boost the CO<sub>2</sub> electroreduction current density of M-N/C single-atom catalysts to the industrial application level, *Energy Environ. Sci.* 14 (2021) 2349–2356, <https://doi.org/10.1039/d0ee04052e>.
- [30] X. Li, W. Bi, M. Chen, Y. Sun, H. Ju, W. Yan, J. Zhu, X. Wu, W. Chu, C. Wu, Y. Xie, Exclusive Ni-N<sub>4</sub> sites realize near-unity CO selectivity for electrochemical CO<sub>2</sub> reduction, *J. Am. Chem. Soc.* 139 (2017) 14889–14892, <https://doi.org/10.1021/jacs.7b09074>.
- [31] S. Li, M. Ceccato, X. Lu, S. Frank, N. Lock, A. Roldan, X.-M. Hu, T. Skrydstrup, K. Daasbjerg, Incorporation of nickel single atoms into carbon paper as self-standing electrocatalyst for CO<sub>2</sub> reduction, *J. Mater. Chem. A* 9 (2021) 1583–1592, <https://doi.org/10.1039/d0ta08433f>.
- [32] S. Liang, L. Huang, Y. Gao, Q. Wang, B. Liu, Electrochemical reduction of CO<sub>2</sub> to CO over transition metal/N-doped carbon catalysts: the active sites and reaction mechanism, *Adv. Sci.* 8 (2021), e2102886, <https://doi.org/10.1002/advs.202102886>.
- [33] T. Zheng, K. Jiang, N. Ta, Y. Hu, J. Zeng, J. Liu, H. Wang, Large-scale and highly selective CO<sub>2</sub> electrocatalytic reduction on nickel single-atom catalyst, *Joule* 3 (2019) 265–278, <https://doi.org/10.1016/j.joule.2018.10.015>.
- [34] K. Jiang, S. Siahrostami, T. Zheng, Y. Hu, S. Hwang, E. Stavitski, Y. Peng, J. Dines, M. Gangisetty, D. Su, K. Attenkofer, H. Wang, Isolated Ni single atoms in graphene nanosheets for high-performance CO<sub>2</sub> reduction, *Energy Environ. Sci.* 11 (2018) 893–903, <https://doi.org/10.1039/c7ee03245e>.
- [35] Y. Cheng, S. Zhao, B. Johannessen, J.P. Veder, M. Saunders, M.R. Rowles, M. Cheng, C. Liu, M.F. Chisholm, R. De Marco, H.M. Cheng, S.Z. Yang, S.P. Jiang, Atomically dispersed transition metals on carbon nanotubes with ultrahigh loading for selective electrochemical carbon dioxide reduction, *Adv. Mater.* 30 (2018), 1706287, <https://doi.org/10.1002/adma.201706287>.
- [36] Y. Cheng, S. Zhao, H. Li, S. He, J.-P. Veder, B. Johannessen, J. Xiao, S. Lu, J. Pan, M.F. Chisholm, S.-Z. Yang, C. Liu, J.G. Chen, S.P. Jiang, Unsaturated edge-anchored Ni single atoms on porous microwave exfoliated graphene oxide for electrochemical CO<sub>2</sub>, *Appl. Catal. B* 243 (2019) 294–303, <https://doi.org/10.1016/j.apcatb.2018.10.046>.
- [37] L. Zhao, Y. Zhang, L.B. Huang, X.Z. Liu, Q.H. Zhang, C. He, Z.Y. Wu, L.J. Zhang, J. Wu, W. Yang, L. Gu, J.S. Hu, L.J. Wan, Cascade anchoring strategy for general mass production of high-loading single-atomic metal-nitrogen catalysts, *Nat. Commun.* 10 (2019) 1278, <https://doi.org/10.1038/s41467-019-09290-y>.
- [38] Y. Xiong, W. Sun, Y. Han, P. Xin, X. Zheng, W. Yan, J. Dong, J. Zhang, D. Wang, Y. Li, Cobalt single atom site catalysts with ultrahigh metal loading for enhanced aerobic oxidation of ethylbenzene, *Nano Res.* 14 (2021) 2418–2423, <https://doi.org/10.1007/s12274-020-3244-4>.
- [39] C. Xia, Y. Qiu, Y. Xia, P. Zhu, G. King, X. Zhang, Z. Wu, J.Y.T. Kim, D.A. Cullen, D. Zheng, P. Li, M. Shakouri, E. Heredia, P. Cui, H.N. Alshareef, Y. Hu, H. Wang, General synthesis of single-atom catalysts with high metal loading using graphene

- quantum dots, *Nat. Chem.* 13 (2021) 887–894, <https://doi.org/10.1038/s41557-021-00734-x>.
- [40] D. Malko, A. Kucernak, T. Lopes, In situ electrochemical quantification of active sites in Fe–N/C non-precious metal catalysts, *Nat. Commun.* 7 (2016), 13285, <https://doi.org/10.1038/ncomms13285>.
- [41] G. Bae, H. Kim, H. Choi, P. Jeong, D.H. Kim, H.C. Kwon, K.S. Lee, M. Choi, H.S. Oh, F. Jaouen, C.H. Choi, Quantification of active site density and turnover frequency: from single-atom metal to nanoparticle electrocatalysts, *JACS Au* 1 (2021) 586–597, <https://doi.org/10.1021/jacsau.1c00074>.
- [42] B. Ravel, M. Newville, ATHENA, ARTEMIS, HEPHAESTUS: data analysis for X-ray absorption spectroscopy using IFEFFIT, *J. Synchrotron Radiat.* 12 (2005) 537–541, <https://doi.org/10.1107/S0909049505012719>.
- [43] S.I. Zabinsky, J.J. Rehr, A. Ankudinov, R.C. Albers, M.J. Eller, Multiple-scattering calculations of x-ray-absorption spectra, *Phys. Rev. B* 52 (1995) 2995–3009, <https://doi.org/10.1103/PhysRevB.52.2995>.
- [44] X.S. Zhao, F. Su, Q. Yan, W. Guo, X.Y. Bao, L. Lv, Z. Zhou, Templating methods for preparation of porous structures, *J. Mater. Chem.* 16 (2006) 637–648, <https://doi.org/10.1039/b513060c>.
- [45] H.B. Yang, S.-F. Hung, S. Liu, K. Yuan, S. Miao, L. Zhang, X. Huang, H.-Y. Wang, W. Cai, R. Chen, J. Gao, X. Yang, W. Chen, Y. Huang, H.M. Chen, C.M. Li, T. Zhang, B. Liu, Atomically dispersed Ni(I) as the active site for electrochemical CO<sub>2</sub> reduction, *Nat. Energy* 3 (2018) 140–147, <https://doi.org/10.1038/s41560-017-0078-8>.
- [46] J. Yang, Z. Qiu, C. Zhao, W. Wei, W. Chen, Z. Li, Y. Qu, J. Dong, J. Luo, Z. Li, Y. Wu, In situ thermal atomization to convert supported nickel nanoparticles into surface-bound nickel single-atom catalysts, *Angew. Chem. Int. Ed.* 57 (2018) 14095–14100, <https://doi.org/10.1002/anie.201808049>.
- [47] D. Xi, J. Li, J. Low, K. Mao, R. Long, J. Li, Z. Dai, T. Shao, Y. Zhong, Y. Li, Z. Li, X. J. Loh, L. Song, E. Ye, Y. Xiong, Limiting the uncoordinated N species in M–Nx single-atom catalysts toward electrocatalytic CO<sub>2</sub> reduction in broad voltage range, *Adv. Mater. Interfaces* 34 (2021), 2104090, <https://doi.org/10.1002/adma.202104090>.
- [48] X. Cao, L. Zhao, B. Wulan, D. Tan, Q. Chen, J. Ma, J. Zhang, Atomic bridging structure of nickel-nitrogen-carbon for highly efficient electrocatalytic reduction of CO<sub>2</sub>, *Angew. Chem. Int. Ed.* 61 (2021), e202113918, <https://doi.org/10.1002/anie.202113918>.
- [49] C.W. Lee, N.H. Cho, S.W. Im, M.S. Jee, Y.J. Hwang, B.K. Min, K.T. Nam, New challenges of electrokinetic studies in investigating the reaction mechanism of electrochemical CO<sub>2</sub> reduction, *J. Mater. Chem. A* 6 (2018) 14043–14057, <https://doi.org/10.1039/c8ta03480j>.
- [50] J. Gu, C.-S. Hsu, L. Bai, H.M. Chen, X. Hu, Atomically dispersed Fe-3+ sites catalyze efficient CO<sub>2</sub> electroreduction to CO, *Science* 364 (2019) 1091–1094, <https://doi.org/10.1126/science.aaw7515>.
- [51] S. Zhu, B. Jiang, W.B. Cai, M. Shao, Direct observation on reaction intermediates and the role of bicarbonate anions in CO<sub>2</sub> electrochemical reduction reaction on Cu surfaces, *J. Am. Chem. Soc.* 139 (2017) 15664–15667, <https://doi.org/10.1021/jacs.7b10462>.
- [52] S. Zhao, Y. Cheng, J.-P. Veder, B. Johannessen, M. Saunders, L. Zhang, C. Liu, M. F. Chisholm, R. De Marco, J. Liu, S.-Z. Yang, S.P. Jiang, One-Pot pyrolysis method to fabricate carbon nanotube supported Ni single-atom catalysts with ultrahigh loading, *ACS Appl. Energy Mater.* 1 (2018) 5286–5297, <https://doi.org/10.1021/acsaem.8b00903>.
- [53] C. Lu, J. Yang, S. Wei, S. Bi, Y. Xia, M. Chen, Y. Hou, M. Qiu, C. Yuan, Y. Su, F. Zhang, H. Liang, X. Zhuang, Atomic Ni anchored covalent triazine framework as high efficient electrocatalyst for carbon dioxide conversion, *Adv. Funct. Mater.* 29 (2019), 1806884, <https://doi.org/10.1002/adfm.201806884>.
- [54] S. Liu, H.B. Yang, S.F. Hung, J. Ding, W. Cai, L. Liu, J. Gao, X. Li, X. Ren, Z. Kuang, Y. Huang, T. Zhang, B. Liu, Elucidating the electrocatalytic CO<sub>2</sub> reduction reaction over a model single-atom nickel catalyst, *Angew. Chem. Int. Ed.* 59 (2020) 798–803, <https://doi.org/10.1002/anie.201911995>.
- [55] X. Rong, H.J. Wang, X.L. Lu, R. Si, T.B. Lu, Controlled synthesis of a vacancy-defect single-atom catalyst for boosting CO<sub>2</sub> electroreduction, *Angew. Chem. Int. Ed.* 59 (2020) 1961–1965, <https://doi.org/10.1002/anie.201912458>.
- [56] J.F. Xie, X.Y. Wang, J.Q. Lv, Y.Y. Huang, M.X. Wu, Y.B. Wang, J.N. Yao, Reversible aqueous Zinc-CO<sub>2</sub> batteries based on CO<sub>2</sub>-HCOOH interconversion, *Angew. Chem. Int. Ed.* 57 (2018) 16996–17001, <https://doi.org/10.1002/anie.201811853>.